Pedestrian dynamics at the running of the bulls evidence an inaccessible region in the fundamental diagram

Daniel R. Parisi[a,1], Alan G. Sartorio[b], Joaquín R. Colonnello[b], Angel Garcimartín[c], Luis A. Pugnaloni[d], and Iker Zuriguel[c]

[a]Centro de Agentes Físicos, Bilógicos y Sociales, Instituto Tecnológico de Buenos Aires (ITBA), Consejo Nacional de Investigaciones Científicas y Técnicas, 1437 C. A. de Buenos Aires, Argentina; [b]Departmento de Ingeniería Informática, Instituto Tecnológico de Buenos Aires (ITBA), 1437 C. A. de Buenos Aires, Argentina; [c]Departamento de Física y Matemática Aplicada, Facultad de Ciencias, Universidad de Navarra, E-31080 Pamplona, Spain; and [d]Departamento de Física, Facultad de Ciencias Exactas y Naturales, Universidad Nacional de La Pampa, Consejo Nacional de Investigaciones Científicas y Técnicas, 6300 Santa Rosa, Argentina

Edited by Iain D. Couzin, Max-Planck-Gesellschaft, Konstanz, Germany, and accepted by the Editorial Board October 4, 2021 (received for review April 28, 2021)

We characterize the dynamics of runners in the famous "Running of the Bulls" Festival by computing the individual and global velocities and densities, as well as the crowd pressure. In contrast with all previously studied pedestrian systems, we unveil a unique regime in which speed increases with density that can be understood in terms of a time-dependent desired velocity of the runners. Also, we discover the existence of an inaccessible region in the speed–density state diagram that is explained by falls of runners. With all these ingredients, we propose a generalization of the pedestrian fundamental diagram for a scenario in which people with different desired speeds coexist.

pedestrian dynamics | fleeing behavior | fundamental diagram | high-speed pedestrians

The world-famous Running of the Bulls (San Fermín) Festival constitutes a unique system of pedestrians running away from bulls in the streets of Pamplona (Spain). Curiously, despite that this race has been repeatedly used as an illustration of competitive pedestrian dynamics, it has not been studied in detail until now. Runners, first waiting for and then escaping from bulls, constitute a fascinating annual scenario of real fleeing pedestrians, becoming an invaluable opportunity for studying and understanding extreme pedestrian dynamics.

One of the main macroscopic observables for characterizing pedestrian systems is the fundamental diagram derived from the speed–density relation for a group of moving pedestrians (1–16). This relation, which is used as a benchmark in design and planning (17–20), accounts for the accepted fact that the speed of the group decreases monotonically as the density increases. Under ordinary conditions, this behavior can be explained because people try to avoid physical contact and slow down when the available space reduces. A key feature of this plot is the speed at near-zero density, which indicates the velocity at which pedestrians would move if they were alone. This speed is known as the desired speed or the free speed (v_0).

Given their importance, speed–density relations are widely studied in the literature; however, most of the existing investigations assume implicitly two essential facts:

- All pedestrians have constant desired speed normally distributed with small variance (an exception to this is the time-dependent desired speed implemented in ref. 21).
- The speed–density relations correspond to stationary (or quasi-stationary) pedestrian systems.

Importantly, these premises hold even for the fundamental diagrams obtained in extreme conditions. As examples, we highlight the fundamental diagram for running pedestrians at medium speed (16), the empirical results collected in a real event (8), and the outcomes obtained in highly competitive evacuation drills in which pedestrians were allowed to push each other (22). In these last two cases, very high densities were present (which dominate the dynamics) and the free velocities were below 1.5 m/s. Remarkably, the assumptions used for traditional fundamental diagrams are not valid in the Running of the Bulls Festival. Here, a moving threat (the bulls) induces time-dependent desired velocities along with a broad distribution among individuals. To understand the complicated dynamics observed, we characterize this system by studying—among other variables—the speed, density, and falling probability of the pedestrians.

The Pedestrian System

During the week of the San Fermín festival, there is a bull run ("encierro") every morning through the streets of Pamplona. The course is 875 m long, starting in a yard, and finishing in the bullring (see map in ref. 23). There, people run in front of six fighting bulls that are accompanied by six tamed bell oxen. Although the distance is not too long, it is impossible for a runner to cover the whole course for several reasons, such as the presence of other runners and, above all, the high speed of the bulls (the mean speed of the bulls, in our measurement areas, is 6 m/s).

Significance

A topic of special interest in crowd dynamics that can lead to better infrastructure management is the study of people under high competitiveness. Persons fleeing from real danger is one instance of this scenario, but of course it is difficult to analyze it experimentally. This is why people running with bulls at the San Fermín Festival provides an exceptional annual event where real data of pedestrian dynamics under extreme conditions can be collected. This kind of data is scarce and therefore highly valuable.

Author contributions: D.R.P., A.G., and L.A.P. designed video acquisition system; D.R.P. recorded videos; A.G.S. and J.R.C. developed tracking software; D.R.P., A.G.S., and J.R.C. processed images; D.R.P. and I.Z. analyzed data; D.R.P., A.G., L.A.P., and I.Z. wrote the paper; and D.R.P. made simulations.

The authors declare no competing interest.

This article is a PNAS Direct Submission. I.D.C. is a guest editor invited by the Editorial Board.

[1]To whom correspondence may be addressed. Email: dparisi@itba.edu.ar.

This article contains supporting information online at https://www.pnas.org/lookup/suppl/doi:10.1073/pnas.2107827118/-/DCSupplemental.

Published December 6, 2021.

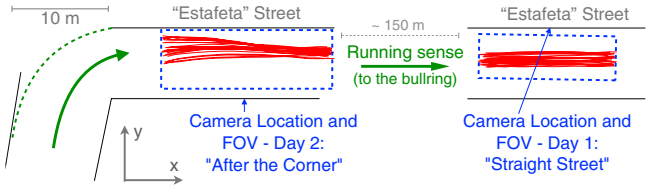

Fig. 1. Layout of the street and locations where the videos were recorded on 8 July (day 1) and 9 July (day 2). Dashed rectangles indicate the FOV of the camera. Blue arrows indicate the camera position. Red lines show recorded bull trajectories (heads and tails).

We recorded two of these runs on consecutive days (8 and 9 July 2019) at two different locations in Estafeta Street. This 300-m-long street is the most famous in the bull run and is characterized by being relatively narrow (around 7 m wide). It starts at a corner; we have taken one recording 10 m after it and another one at about the middle of the street length. Both locations and the corresponding field of view (FOV) are shown in Fig. 1.

Trajectories of individual bulls and runners were extracted from the recorded videos (*Materials and Methods* and Datasets S6–S12). Bulls were marked as six human-equivalent positions (the mass of a bull is similar to the mass of six runners): one on the head, one on the beginning of the tail, and the rest on top of each leg (two over the scapulae and two over the hips). These six points were taken as six virtual humans when calculating the densities of neighbor runners, but were not considered in any other calculation performed in this work. The computed speeds, densities, and other related quantities all correspond only to the runners.

To understand the results, it is important to know the proceedings of the festival. People are admitted into the premises at 7:15 AM, and they wait there for 45 min. We have called this state S_A, in which runners first remain in place, at high density, and then walk slowly (see the x-velocity distributions, v_x, in Fig. 2*A* and Movie S1 [https://osf.io/pu35r/]). At 8:00 AM the bullring door—at the end of the course—is open, and a sizable portion of the people walk into it, so that only some runners remain in the path waiting for the bulls. The street becomes less congested and, occasionally, runners are seen to warm up (Fig. 2*B*, system

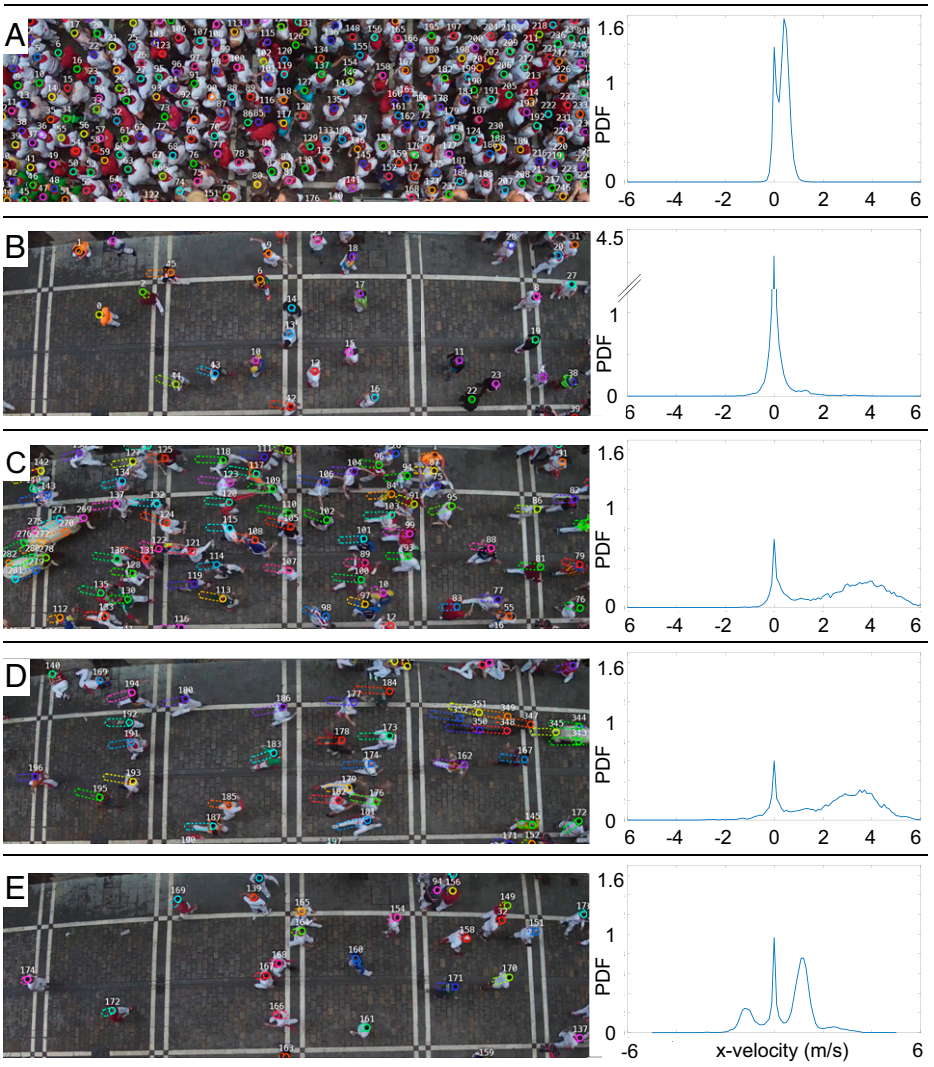

Fig. 2. States of the pedestrian system. (*A*) State S_A. (*B*) State S_B. (*C*) State S_C. (*D*) State S_D. (*E*) State S_E. See text for description of the states. In the snapshots (*A–E*, *Left*), labels indicate the pedestrian number, the circles mark the actual position of runners, and the dotted lines show the distance traveled by runners in a time lapse of 0.13 s (*Materials and Methods*). Bulls are indicated by six runner-equivalent circles. Consider shoulder width (~0.4 m) as distance reference. (*A–E*, *Right*) The PDF of the x component of the velocity is displayed for each state.

state S_B). Then, a few seconds before the bulls arrive, a shock wave of running pedestrians at high velocity is observed. This shockwave triggers the starting of the race of the waiting runners. This behavior nicely correlates with the velocity distributions displayed in Fig. 2*C*, which show two clear peaks at $v_x = 0$ and $v_x \approx 3.5$ m/s, corresponding to what we have called state S_C. Once the bulls along with the runners in front of them have passed by, a wake of runners with decreasing speed is observed (Fig. 2*D*, state S_D). In about 40 or 50 s the system relaxes toward a situation of normal walking on a pedestrian street, eventually perturbed by lonely runners jogging at medium speed (Fig. 2*E*, state S_E). In summary, depending on the instant of the race, the PDF (probability density function) of the *x* velocity displays peaks of different widths at four distinct positions corresponding to groups of people with different desired speeds, which is relevant for the forthcoming analysis. Finally, 2 min after the beginning of the race, four extra tamed bell oxen run along the path with the purpose of guiding a possible delayed bull to the bullring.

Results

Time Evolution of Macroscopic Observables. We start by analyzing several macroscopic quantities averaged over all the $n_j(t)$ pedestrians present in each time frame (t). In particular, we calculate the mean speed $< v > (t) = \frac{\sum_{j=1}^{n_j(t)} v_j(t)}{n_j(t)}$, the mean density $< \rho > (t) = \frac{\sum_{j=1}^{n_j(t)} \rho_j(t)}{n_j(t)}$, and the mean pedestrian pressure $< P > (t) = \frac{\sum_{j=1}^{n_j(t)} P_j(t)}{n_j(t)}$. Described in refs. 8 and 22, P_j is the local crowd pressure $P_j = \rho_j \mathrm{Var}(v_j, knn)$ computed with the variance of the velocity over the $k = 5$ nearest neighbors for each pedestrian j (which are the same ones used to calculate the individual densities as explained in *Materials and Methods*). In Fig. 3 we display the time evolution of these variables only for the region just after the corner (similar results are obtained at the middle of the straight street). Interestingly, all quantities present a remarkable growth when the first bull enters in the field of view (defined as $t = 0$) followed by a relaxation that is rather quick for density and pressure. The relaxation seems to be slower for the case of velocity: Even well after the passage of the last bull of the first group (second vertical dashed line) it seems that there is a wake of people running quite fast following the bulls toward the bullring. The passage of the later four tamed bell oxen (second pair of vertical dashed lines) also displays a small growth of the velocity and pressure values. The low densities at which this last event occurs evidence that it is not appealing to runners. The values reported in Fig. 3*B* clearly correlate with the occurrence of the four last states described in Fig. 2 (S_B to S_E). State S_A (corresponding to normal walking and people waiting) took place several minutes before and is not included in these time series. The mean of the absolute value of the *y* component of the velocity displayed in Fig. 3*B*, which captures the occurrence of lateral movements, also presents a maximum when the bulls pass through the analyzed region. This feature correlates with a well-known runner strategy that consists of stepping aside when they are not able to keep up with the bulls' pace.

Beyond all the features described above, the most striking behavior of the bull run in the context of pedestrian dynamics is that the speed and density increase simultaneously, in clear contrast with the traditional fundamental diagrams reported in the literature. Therefore, we further look into this phenomenon by representing the speed–density relation of the averaged observables (Fig. 4), keeping the time information in the color code of the curve. Measurements at both locations along the street reveal similar behaviors. The initial state (S_B) can be identified at the beginning as a dark blue curve in the density range $\rho \in (0.4, 0.6)$ m^{-2} and mean speed around $< v > \sim 0.3$ m/s. As explained, this corresponds to runners waiting for the bulls at a fixed positions and occasionally jogging toward another location. As bulls come closer (state S_C), the mean speed increases up to a maximum (around 4 m/s) at which the density also reaches its highest value (around 1 pedestrian per square meter). After this, the system relaxes toward a normal walking situation with mean speed around $< v > \sim 1$ m/s, perturbed only when the second four-bull pack passes, displaying a velocity peak at lower densities. We emphasize that only pedestrian data were used for computing these quantities.

Despite the complicated dynamics, if we look only at the speed–density relation, it is evident that the general rule of decreasing speed when the pedestrian density increases is not fulfilled. Noteworthy, a monotonically decreasing speed–density relation has been consistently observed in dozens of different

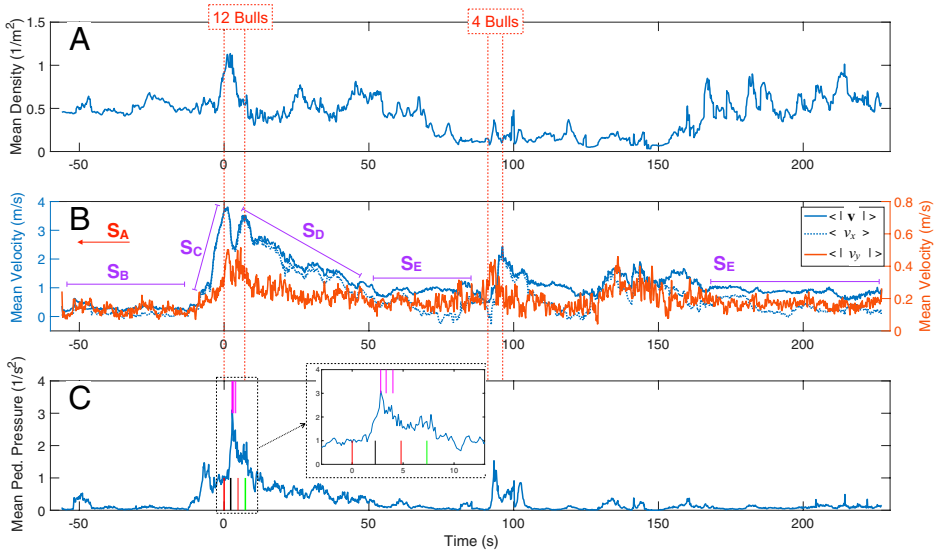

Fig. 3. Time series measured in the region after the corner. (*A*) Mean density. (*B*) Mean velocities (v,v_x,$|v_y|$). The states of the system S_B to S_E identified in Fig. 2 are indicated in purple. The two pairs of vertical red lines indicate the passage of the first 12 bulls and the later 4 tamed bell oxen. (*C*) Mean pedestrian pressure. Events of falling runners are indicated with vertical colored lines; the same color indicates correlated fallings. *Inset* corresponds to the passage of the bulls and the 2 s before it.

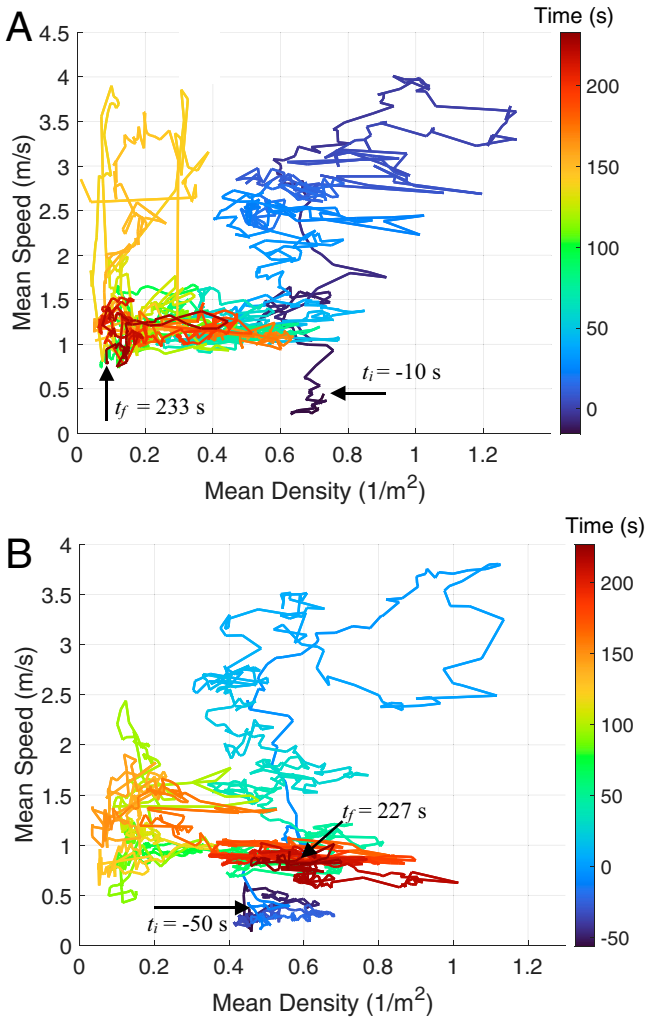

Fig. 4. Mean speed–density diagram. (*A*) In the middle of the straight street. (*B*) In the region "after the corner." The time evolution is encoded by colors as indicated in the color bars.

scenarios, including competitive situations (8, 22). Therefore, this speed–density relation seems to deviate from the general rule. Of course, several differences can be outlined between the bull run and most pedestrian systems. The first one is that in this case, the process is nonstationary as the irruption of bulls introduces a big perturbation in the system. Another one concerns the willingness of pedestrians to run in front of the bulls. Finally, it should be also noted that, if we consider the whole process, a wide range of desired velocities are present in the system. Therefore, in the following section, we investigate this problem by analyzing the speed–density relation from a microscopic point of view.

Untangling the San Fermín Speed–Density Relation. In Fig. 5*A*, we represent with gray dots the values of velocity versus density, as calculated at the individual runner level (*Materials and Methods*) in all the frames registered at both street locations, as indicated in Fig. 1, and including those in the state S_A (which were not present in the time series). Contrary to the observation made in the mean speed–density diagram for states S_B to S_E (Fig. 4), when including state S_A the data cloud seems to suggest a reduction of the velocity as the density increases. Also, it is interesting to note that the points cluster in two overlapping but well-differentiated groups: one for low densities ($\rho < 2$ m^{-2}) where the velocities span from 0 to 7 m/s that in Fig. 5*A* appears as a vertical cloud of points and the other for high densities ($\rho > 2$ m^{-2}) where the velocities are always smaller than 1.5 m/s and in Fig. 5*A* appears as a cloud of points with an envelope that has a slightly decreasing slope. There is a depleted region in the speed–density plane: Runners struggle to reach velocities above 1.5 m/s when $\rho > 2$ m^{-2}. Interestingly, within all the data points represented in Fig. 5*A*, we can distinguish very different pedestrian behaviors depending on the runner analyzed and the specific state of the race as described above. As an example, in Fig. 5*A* we show three characteristic trajectories in the speed–density space (each one corresponds to a different pedestrian). Among the trajectories, we can distinguish a "standard" one occurring at high densities in which the speed reduces as the density increases. Nevertheless, there are other (less common) trajectories where we observe a wide range of speed values for the same or similar (low) densities. This behavior is a piece of clear evidence that pedestrians may change their desired speed with time. For example, pedestrians waiting for the bulls have zero desired speed and, as the bulls come closer, they begin to run, raising the desired speed up to the maximum.

To classify the different behaviors, we perform a principal component analysis (PCA) for each trajectory in the speed–density space and use the slope (m) of the first direction vector as a classification parameter. This direction is the one that maximizes the variance of the data (24). Examples of these vectors are shown in Fig. 5*A* as dashed lines along with their slope values. Then, we choose three groups of pedestrians: 1) Pedestrians with $m \in [-1, 0]$ are said to display "normal behavior" since the speed decreases when the density grows; 2) pedestrians showing $m \in [1, 10]$ are considered to be in an "atypical" scenario because the speed increases with increasing density; 3) and finally, when $|m| > 10$, we have pedestrians in an "extreme condition" as there is an important variation of speed for a rather constant density value.

Next, in Fig. 5 *B–D*, we represent the data points of the speed–density relation that correspond to each class (normal, atypical, and extreme, respectively). Fig. 5*B* reveals that almost all data in the speed–density relation for which $\rho > 2$ m^{-2} correspond to pedestrians displaying normal behavior. On the contrary, a small portion of the data obtained for small values of ρ corresponds to this class of motion. Considering only pedestrians displaying normal behavior, we group individual trajectories according to the speed v_0 at their minimum density (this can be seen as an approximation of the free speed for each given trajectory). Then, we implement a moving average of the data corresponding to each subgroup, obtaining the results represented in Fig. 5*B*. In most cases, the relation is consistent with the traditional negative slope encountered in the literature. However, as the free speed values increase, it is more likely to find almost horizontal curves indicating a constant speed independent of the density. It is reasonable to think that for high competitiveness, as the moving threat approaches, runners want to maintain the maximum speed no matter the density. Also, it is interesting to note that the curves corresponding to $0 \leq v_0 \leq 1$ m/s and $1 \leq v_0 \leq 2$ m/s are clearly distinguishable when the density is smaller than 2 m^{-2}, but coincide for higher densities. This feature—already reported for pedestrian dynamics (7, 16) and in a system involving cars and lorries (25)—suggests that the desired speed has a crucial role in the dynamics observed in dilute conditions, but it becomes less relevant as the density increases. Although our data at high density correspond to state S_A (people with slow desired velocity), in other systems the zone of high density and low speed could display a particular regime of people pushing each other that can cause instabilities, as observed in experiments (22, 26) and turbulent flows as reported for crowd catastrophes (8, 27).

In Fig. 5*C* we show a similar analysis to the one implemented for normal conditions, but for the atypical condition. In this case, the cloud of gray dots shows that the atypical behavior always

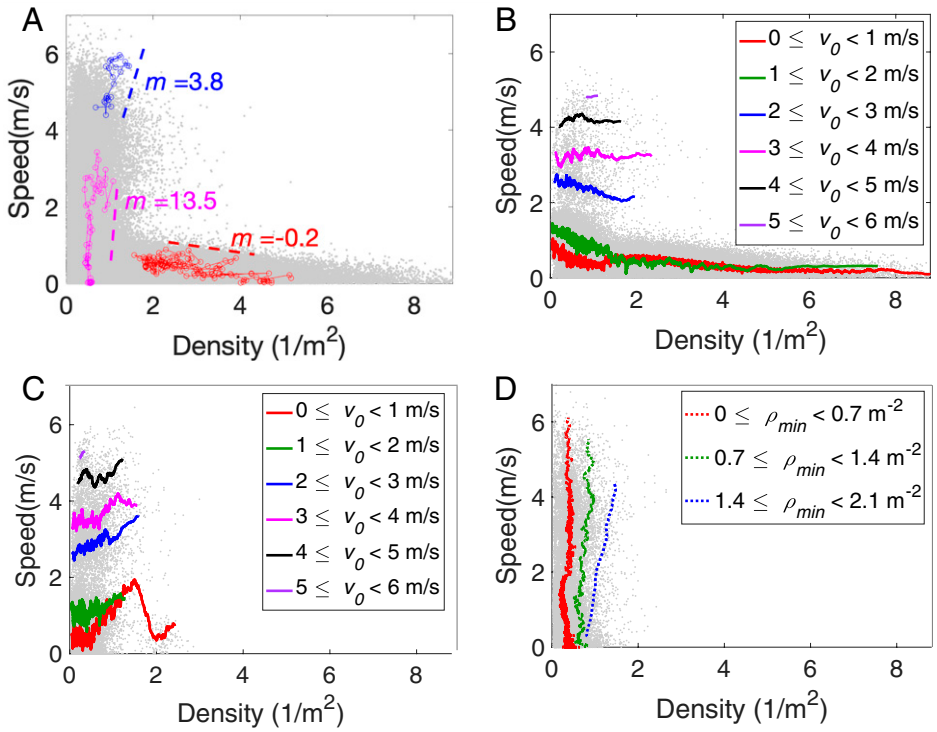

Fig. 5. Microscopic speed–density data points. (*A*) Gray dots represent all pedestrian data obtained from the whole race for the two recorded locations. Solid colors, three examples of individual pedestrian trajectories in the speed–density space. The dashed lines and the *m* value in their corresponding color display the slope of the principal component vector for each trajectory. (*B*) Speed–density data for pedestrian showing normal behavior (i.e., $m \in [-1, 0]$) and the corresponding speed–density curves obtained by computing the moving average of the data when grouped according to its speed at minimum density as indicated in the key. (*C*) Speed–density data for pedestrian showing atypical behavior (i.e., $m \in [1, 10]$) and the corresponding speed–density curves obtained as a moving average of the data, when classified according to its speed at minimum density as indicated in the key. (*D*) Speed–density data for pedestrian showing extreme behavior (i.e., $|m| > 10$) and the corresponding speed–density curves obtained by performing a moving average of the data when classified according to its density at minimum velocity as indicated in the key.

corresponds to situations of low density ($\rho < 2$ m^{-2}). Again, if we group runners according to their speeds v_0 at minimum density, we observe a consistent set of features, for instance that the curves display positive slopes and separation between them (with the only exception of the two obtained for the smallest values of v_0). All these characteristics, together with the weak dependence of the speed on the density observed for low density values and high desired speeds shown in Fig. 5*B*, strongly suggest that the only parameter governing the runners' behavior in dilute conditions is their desired speed.

Finally, the extreme scenario of pedestrians displaying $|m| > 10$ is, as expected, observed in the region of $\rho < 2$ m^{-2} (Fig. 5*D*). In this case, as trajectories are almost vertical, the moving average is computed along the speed axes, grouping trajectories depending on the value of their minimum density. As in the atypical scenario described above, the observed behavior would correspond to pedestrians changing their desired speed for near-constant density values. Nevertheless, the fact that the slopes in the speed–density relation reduce as the initial density augments suggests that pedestrians' ability to reach very high velocities diminishes as the density grows. Indeed, this result supports the previously mentioned idea of the existence of a inaccessible region in the speed–density diagram (speeds above 1.5 m/s and $\rho > 2$ m^{-2}).

The Inaccessible Region in the Speed–Density Relation. In this section we delve into the existence of the inaccessible region of the speed–density space. The question is whether the absence of data for speeds above 1.5 m/s and $\rho > 2$ m^{-2} has a psychological reason (i.e., people voluntarily decide to avoid running at high densities) or, otherwise, if there is any physical constraint that prevents the entry into this area of the parameter space. To shed light on this we have carefully analyzed the falls of the runners, because we have realized that a remarkable proportion of these incidents coincide with the passage of the bulls (which is the situation of higher speed and density).

Indeed, the events with multiple falling people have paramount importance because they can trigger massive pile-ups that may cause a large number of casualties. Several falls involving a large number of persons have occurred in previous years, mainly at the narrowest part of the path (the entrance of the bullring), as in 1957 (28) and 1977 (29) or more recently in 2013 (30). Although these big pile-ups are sporadic, single falls or small-group falls are more frequent, and some instances were seen in our recordings. In particular, we observed a total of 20 people falling, 13 on the first day and 7 on the second day. All of them took place during the passage of the bulls, coinciding with a scenario of high average density, velocity, and crowd pressure, as shown with vertical colored lines in Fig. 3*C* for day 2 (the same occurs for day 1). This seems a piece of additional evidence in favor of the hypothesis of Helbing et al. (8) who proposed that the crowd pressure can be correlated with the probability of falling.

Indeed, it is natural to assume that the first falling and the consecutive ones will occur with increasing probability when augmenting both the crowd speed variance and density. Less available space can cause accidental physical contact of runners, which may affect their motion and trigger their falling. Therefore, the probability of falling in the bull run will vary drastically over time, being significant only in the transition between states S_C and S_D coinciding with the bulls' passage. But in addition to

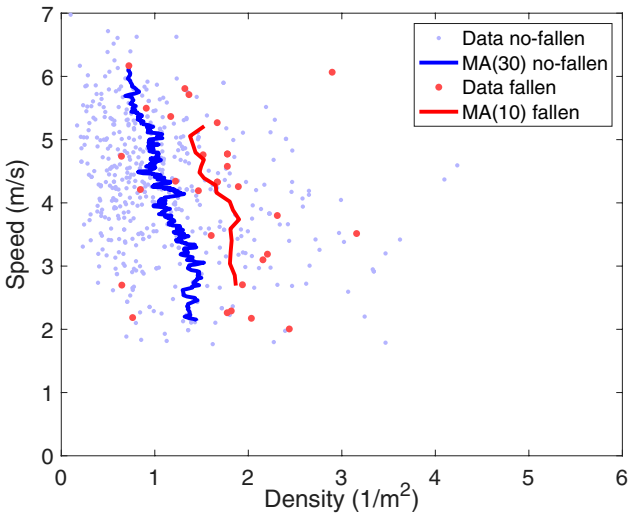

Fig. 6. Microscopic speed–density data for pedestrians identified at the time of the bulls' passage. For each pedestrian, two points are represented, one for the pedestrian's maximum velocity and another for the pedestrian's maximum local density. Red and blue dots represent data for pedestrians that fall and do not fall, respectively, as indicated in the key. In the case of falling, the data belong to the trajectories before the falling event. Red and blue solid lines represent the moving averages (MA) along the speed axis computed for each case.

this, the falling probability will also depend on, for example, the occurrence of a previous fall, i.e., the presence of a runner on the ground. Indeed, it is interesting to note that only 6 falls were independent (uncorrelated) whereas 14 of them belonged to a small-group fall. Although our sample size is small, we estimate a falling probability by counting the ratio between the number of falls and the number of runners between the first and last of the 12-pack bulls. If we include runners from the frame in which the head of the first bull exits the FOV to the frame when the tail of the last bull enters the FOV, we counted 97 runners (both days combined). Thus, the 20 observed falls lead to a falling probability of about 0.21. Note that this value might be likely an overestimation. If we consider instead the interval between the entrance of the first bull in the FOV and the exit of the last one, the fall probability would be 0.08. The data presented in Fig. 6 (blue) correspond to this last computation.

To decide whether there is any relationship between the falling events and the inaccessible region in the speed–density diagram, in Fig. 6 we compare the microscopic speed–density relations for the falling pedestrians with the nonfalling pedestrians. For this comparison, only the data of nonfalling pedestrians that are in the movies during the falling events (i.e., when the bulls cross through the field of view) are considered. In addition, given that falling events are probably related with extreme values of either speed or density, we draw in the plot only two points for each runner: One represents the pedestrian velocity when the density at the pedestrian location is maximum and the other the density at the pedestrian location corresponding to the maximum velocity of that particular pedestrian. Then, we compute the moving averages of each group of data separately (taking the speed axis as the independent variable), evidencing a clear shift toward higher densities for the case of pedestrians that fall. We propose that the moving-average line corresponding to falling pedestrians could be seen as a boundary separating zones of physically allowed speed–densities from another zone in which the pedestrian system would collapse because of the occurrence of falls. Indeed, this hypothesis is supported by the fact that the position of this vertical line seems to coincide with the density and velocity values above which the density of points in the global microscopic speed–density relation is dramatically reduced (Fig. 5*A*).

Another strong argument for the existence of an inaccessible region in the speed–density diagram can be put forward from independent biomechanical arguments if we consider that the higher the runner speed, the more available space is needed to take a step. Indeed, the relation between the runners' speed and their stride length (L_S) has been reported in refs. 31–33. These studies show that the stride length increases with speed as shown in Fig. 7, *Inset*. The maximum local density ρ_i at which a pedestrian can make a stride L_S can be estimated as $\rho_i = 1/(L_S\ W_e)$, with W_e the effective runner width (*SI Appendix*, Fig. S1). Then, using refs. 31–33, we can obtain the minimum space (maximum density) required by runners to take a step, depending on their speed (solid lines in Fig. 7). In other words, these curves separate physically accessible from inaccessible regions in the speed–density diagram. Interestingly, the theoretical limit obtained is close to the empirical boundary marking the zone of the diagram where runners are at a high risk of falling, as shown in Fig. 6.

Encompassing Macroscopic and Microscopic Behavior. After having identified the different types of individual behaviors leading to the microscopic speed–density diagram shown in Fig. 5, we are in a position to explain the origin of the counterintuitive macroscopic speed–density plots displayed in Fig. 4. To this end, knowing the type of individual behavior predominating at each moment becomes crucial. For this reason, in *SI Appendix*, Fig. S2, we report the temporal evolution of the number of pedestrians that belong to the three different types of behavior (normal, atypical, and extreme) together with the different stages of the race depicted in Fig. 2. We further filter these signals considering normal behavior only for pedestrians with $v < 1.7$ m/s and $v > 1.7$ m/s in the other two cases. Clearly, before the approach of the bulls (stage S_B) pedestrians behave normally ($m \in [-1, 0]$), a pattern that is dramatically altered when the animals arrive at the field of view. At this moment (stage S_C), the number of pedestrians behaving normally goes to zero and there is a peak of people showing atypical and extreme behavior. During the next 50 s or so (stage S_D), there is a gradual relaxation of the number of atypical and extreme runners accompanied by a growth in the number of normal pedestrians. After about 50 s (stage S_E), the main observed behavior is the normal one, maybe with a small alteration at ∼100 s, when the second pack of tamed

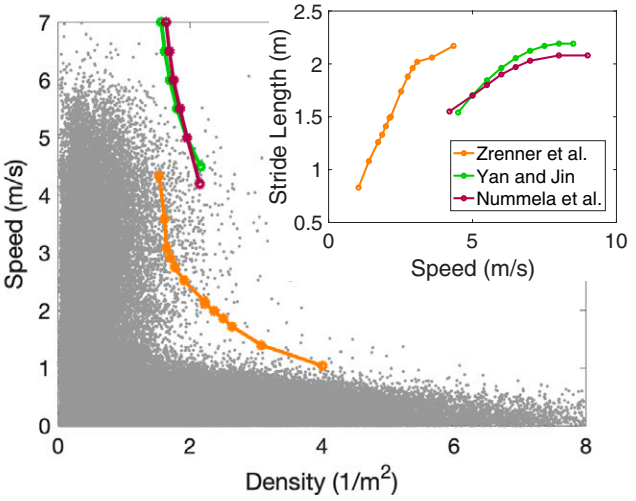

Fig. 7. Theoretical limit in the speed–density diagram given by the biomechanical data of the stride length of runners required for a given speed (main text). Reported data correspond to Zrenner et al. (31), Nummela et al. (32), and Yan and Jin (33).

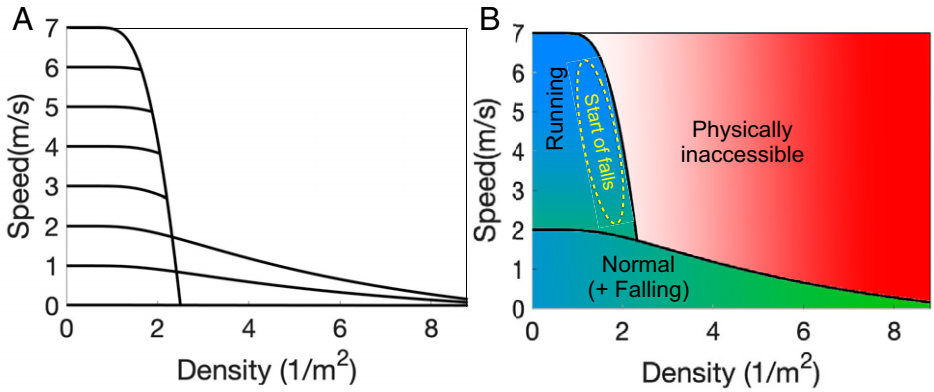

Fig. 8. Hypothetical high-speed fundamental diagram. (*A*) Possible speed–density curves for different desired speeds $v_0 = v(\rho = 0)$ (Eq. **2**). (*B*) Proposed state diagram with, at least, three different regimes.

bell oxen passes through the analyzed region. Note also that, for the high density and noncompetitive condition of the stage S_A (not shown in the graph as it occurs long before the arrival of the bulls), all the individual data fall in the region corresponding to the normal condition where the speed reduces with the density for $\rho > 2\ \mathrm{m}^{-2}$ (*SI Appendix*, Fig. S2, *Inset*).

Overall, we observe normal behavior (i.e., $m \in [-1, 0]$) in most situations with the exception of the time at which the bulls arrive and the 40 to 50 s thereafter. At these stages, the runners display either atypical or extreme behavior, coinciding with the positive correlation of the average velocity and the macroscopic density shown in Fig. 4. If we consider the presence of the bulls as a perturbation similar to the one studied by Nicolas et al. (34), the runners clearly anticipate it and start running. Moreover, the fact that the bulls occupy a big fraction of the available area of the street and the willingness of runners to approach the bulls cause a sudden increase in the density. In this sense, we can state that both pedestrian interactions and the special nature of the perturbation triggering their motion determine the observed dynamics.

Discussion

In this work, we have shown that the speed–density relation in the San Fermín festival does not correspond to any of the fundamental diagrams reported so far for pedestrians in normal or competitive conditions. Indeed, the increase of the average velocity with the systems' average density is at odds with established rules on pedestrian dynamics. Apart from the fact that the running of the bulls is a time-dependent process, we have revealed that the key aspect behind this unusual feature is the variety of ways in which people behave.

Based on the results in the previous sections, we put forward the following explanation for the observed "bull-run" fundamental diagram:

- Instead of a single speed–density relation, there exist many curves that correspond to a broad range of desired speeds. Indeed, as the desired speed grows the curves become flatter for a range of small densities (Fig. 5*B*). This can be explained if one assumes that runners that are at maximum risk have a very high desired speed no matter the density.
- The counterintuitive behavior of increasing speed with increasing density would reflect pedestrians changing between different curves corresponding to different desired speeds. It shows that an important number of pedestrians wait for the arrival of the bulls and at that moment they increase their desired speed, leading to a behavior shown in Fig. 5 *C* and *D*.
- For very fast runners, high local densities increase the danger of falls, a feature that can be rationalized in terms of the stride length dependence on the speed. Therefore, it is reasonable to assume that a physical boundary exists for high speeds and high densities. The red line in Fig. 6 and curves in Fig. 7 give a qualitative idea of the position of this boundary in the speed–density diagram.

In Fig. 8*A* we sketch the different speed–density relations that have been identified. The curves represent particular cases of the Kladek–Newell–Weidmann equation (1, 3, 35), an analytical expression having the flexibility to fit observed speed–density diagrams (*Materials and Methods*). Note that our proposal suggests that the curves corresponding to the highest desired velocities drop to a speed equal to zero for high densities, illustrating the collapse of the system that can be expected when runners try to run too fast in such crowded conditions. Moreover, the curve for $v_0 = 7$ m/s represents a part of the boundary between accessible and inaccessible areas in the speed–density diagram. The lower v_0 curves try to reproduce the experimental ones shown in Fig. 5*B*. The curve for $v_0 = 2$ m/s represents an enveloping curve of the data points displayed as a gray cloud in Figs. 5*A* and 7. Also, it marks the lower boundary of the accessible–inaccessible limit, coinciding with the curve of Zrenner et al. (31) in Fig. 7. The limit $v_0 = 0$ m/s means that if all pedestrians had zero desired speed, the crowd would not move no matter the density.

Regardless of the particular shape of the curves for the various desired speeds, the combination of them will lead to a generalized speed–density space similar to the one sketched in Fig. 8*B*. There, different regions can be distinguished: 1) a fleeing region for low densities in which pedestrians would be able to change their desired velocity and jump between different curves, 2) an inaccessible region for high velocities and densities at which pedestrians would have a high probability of falling, and 3) a normal region for pedestrians with low desired speeds where the speed reduces with increasing density as usually observed in steady-state crowds. Note that in this region walking pedestrians coexist with those that want to run but suffer a fall. This degeneration could be broken if we include the desired speed as a third state variable, which in the case of a falling pedestrian can be approximated by the actual speed at which the falling begins.

To test the above explanation of the peculiar speed–density relation observed in Fig. 4, we carried out simulations for states S_C and S_D. To this end, we used the contractile particle model (36), which has been shown to reproduce the experimental speed–density data for pedestrian systems under normal conditions. Except for the constant desired velocities, all the other parameters of the model are set in the range of those reported in ref. 36. For a description of this model along with its parameters see *SI Appendix*.

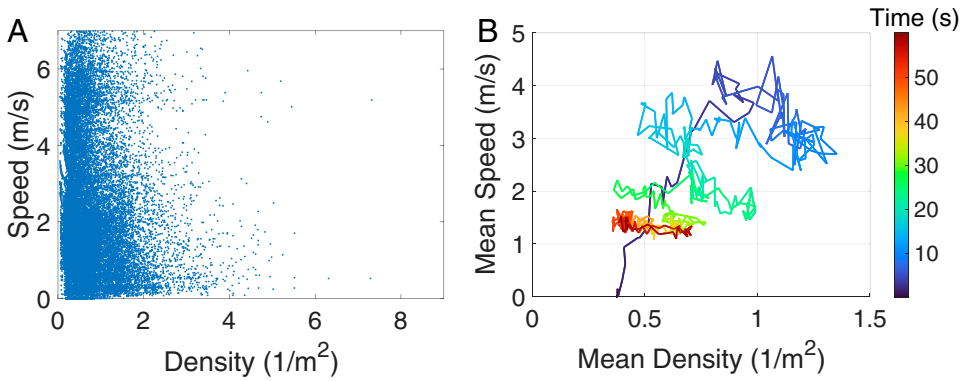

Fig. 9. Simulation results of states S_C and S_D. (*A*) Individual speed–density data. (*B*) Average speed and density in each time frame. The time evolution is encoded in color.

The main aspect that we introduce in the simulations is the time-dependent nature of the desired velocities, which depend on the distance to the bulls. The simulation area has 6 m in width and 18 m in length (*SI Appendix*, Fig. S3). Initially, a set of $n_0 = 40$ waiting agents are distributed uniformly within this area with desired speed $v_0 = 0$ m/s. Three seconds after the simulation starts, a pack of 10 bulls enters the simulation area at a fixed speed $v_b = 6$ m/s. Around the bull pack, a new group of $n_1 = 20$ agents enters the simulation area (this kind of increase in the number of runners was observed in our data; *SI Appendix*, Fig. S4 and Movies S2 [https://osf.io/spgtw/] and S3 [https://osf.io/snhyp/]) and its desired velocities are in the range $v_0 \in (4.8, 6)$ m/s. Each of the n_0 waiting particles activates (i.e., switch its own v_0 to a positive value) when the first bull particle is at a distance (in the x direction) of 9 m from its position. At that moment, the desired speed of the waiting particle changes to a random value $v_0 \in (4.8, 7.2)$ m/s. Agents behind the bulls slow down, changing the desired speed linearly with time until it reaches a walking value in the range $v_0 \in (0.75, 2.25)$ m/s at about 40 s since the simulation started.

The results of the simulations shown in Fig. 9 reproduce the same kind of dynamics as observed in the real system. Fig. 9*A* displays microscopic information of local density and speed. If we compared this cloud of points with the one in Fig. 7 (or Fig. 5*A*), we can observe the equivalent vertical development of the data at low density corresponding to the change of the desired velocities with time. In Fig. 9*B*, the time evolution of the mean speed and density qualitatively matches the results observed in the San Fermín system displayed in Fig. 4 in which the mean speed and density increase simultaneously. It should be noted that the simple model used does not consider falls or avoidance mechanisms. However, the inaccessible region of the speed–density diagram is apparent.

In summary, after recording and analyzing a real and emblematic pedestrian system in which people display several states of behavior including high-speed fleeing from a moving threat, we observed a positive correlation between speed and density that can be explained in terms of time-dependent desired speed, which is determined by the bulls' presence. Furthermore, using this information we postulate a generalization of the traditional fundamental diagram of pedestrian dynamics that encompasses the different behaviors observed.

Materials and Methods

Image Acquisition and Processing. The video camera used was a FLIR DUO PRO R 640 45°FOV and it was placed at ∼15 m over the street floor. Visible and infrared images were taken, but we used only the visible channel that has a resolution of 3,840 × 2,160 pixels and a frame rate of 30 fps (time interval $dt = 1/30$ s). Each image was reduced to 960 × 540 pixels and further cropped to cut off walls and buildings from the image, leaving a final useful image with bulls and pedestrians of about 960 × 350 pixels. Also, the time resolution was reduced to $dt = 4/30$ s $= 0.13$ s when analyzing the images.

The images were processed semiautomatically. For this, we developed an ad hoc software that allows the users to label in subsequent frames each pedestrian head by clicking with the computer mouse on the image and correcting it if necessary. The software can go forward and backward along the recording taking one frame out of every four, effectively reducing the frame rate to $dt = 4/30$ s. The main source of error in the pedestrian location is the size of the pedestrians' heads and their body height. We estimated that this error was about 0.15 m that is reduced to about 0.12 m with smoothing (see below). Once the positions of all runners and bulls were obtained, they were corrected for the lens distortion using the function "undistortPoints" of the OpenCV library (37). We assumed no tangential distortion on the lens and determined the quadratic radial distortion coefficient empirically, using as reference known straight lines in the picture.

Finally, to reduce acquisition fluctuations, the trajectories $x_i'(t)$ and $y_i'(t)$ are smoothed by interpolating them with a generalized regression neural network (GRNN) (38) with spread value $\sigma = 1$.

It must be noted that because of the zenithal camera position, the distance to the people, and the resolution used, the actual identity of each runner is preserved. The "Comité de Ética de la Investigación de la Universidad de Navarra" (Research Ethics Committee of the University of Navarra) has assessed this article and has no ethical objections.

Microscopic Velocity and Density Calculation. From the $x_i(t)$, $y_i(t)$ positions, the velocities were computed as $v_{xi}(t) = \frac{x_i(t) - x_i(t - 0.13\ \mathrm{s})}{0.13\ \mathrm{s}}$ and $v_{yi}(t) = \frac{y_i(t) - y_i(t - 0.13\ \mathrm{s})}{0.13\ \mathrm{s}}$, and the speed as $v(t) = \sqrt{v_x^2(t) + v_y^2(t)}$.

The local density is calculated by means of the nonparametric k-nearest neighbors (k-nn) method already considered for similar systems (39, 40). This method allows computation of the density at any arbitrary point (x, y) in the space. It relies on measuring the distance to the kth nearest neighbor (d_k) of the point (x, y). In our case, we choose the points in space coinciding with each runner i; in consequence, the first neighbor of the space point (x, y) is (x_i, y_i) being at zero distance. Then, the density is computed as $\rho_i = \frac{k-1}{\pi\ d_k^2}$ (*SI Appendix*, Fig. S5). We took $k = 5$. If the circle of radius d_k lies out of the boundary, a correction is made by subtracting the portion of the circle area A_{OUT} lying outside the image (*SI Appendix*, Fig. S5), so the density reads

$$\rho_i = \frac{k - 1}{\pi\ d_k^2 - A_{OUT}}. \quad [1]$$

It must be noted that this definition also works when one or more of the k-nn points correspond to a bull.

We compare this method for calculating local densities with another one considering the Voronoi area for each particle (41) and, for $k = 5$, the differences between the two methods are less than 0.35%.

Kladek–Newell–Weidmann Pedestrian Fundamental Diagram. The curves of the generalized pedestrian fundamental diagram of Fig. 8 have the functional form of the Kladek–Newell–Weidmann formula, as stated in refs. 1, 3, and 35,

$$v(\rho) = v_0(1 - e^{-g(\frac{1}{\rho} - \frac{1}{\rho_{max}})}), \quad [2]$$

where g and ρ_{max} are constants; in particular, ρ_{max} is the density at which the speed drops to zero. The particular values used for curves in Fig. 8 are shown in *SI Appendix*, Table S1.

Data Availability. All study data are included in this article and/or *SI Appendix*. Movies S1–S3 have been deposited in the Open Science Framework (OSF) (Movie S1, https://osf.io/pu35r/; Movie S2, https://osf.io/spgtw/; and Movie S3, https://osf.io/snhyp/).

ACKNOWLEDGMENTS. We acknowledge financial support from Instituto Tecnológico de Buenos Aires Grant ITBACyT 2018-42; Agencia Nacionalde Promoción Científica y Tecnológica, Argentina Grant PID 2015-003; Human Frontier Science Program Research Grant RGP0053/2020; and the Spanish Government through Grant PID2020-114839GB-I00 funded by MCIN/AEI/10.13039/501100011033 (Ministerio de Ciencia e Innovación, Agencia Estatal de Investigación). We are also grateful to Lucas S. Gómez, Tamara Puig, Julian F. Arce Doncella, and Esteban Capolicchio for assistance with the semiautomatic image processing. D.R.P. thanks Hernán J. Gómez and Gracián Garcés Díaz for help in the recording of videos.

1. T. Kretz, An overview of fundamental diagrams of pedestrian dynamics (2019). https://www.researchgate.net/profile/Tobias-Kretz-2/publication/336286296_An_overview_of_fundamental_diagrams_of_pedestrian_dynamics/links/5d99ea63458515c1d39abe71/An-overview-of-fundamental-diagrams-of-pedestrian-dynamics.pdf. Accessed 22 April 2021.
2. R. Aghamohammadi, J. A. Laval, Dynamic traffic assignment using the macroscopic fundamental diagram: A review of vehicular and pedestrian flow models. *Transp. Res. Part B Methodol.* **137**, 99–118 (2020).
3. E. Bosina, *A New Generic Approach to the Pedestrian Fundamental Diagram* (ETH Zurich, 2018), vol. 183.
4. R. Lohner, B. Muhamad, P. Dambalmath, E. Haug, Fundamental diagrams for specific very high density crowds. *Collect. Dyn.* **2**, 1–15 (2018).
5. J. Zhang, *Pedestrian Fundamental Diagrams: Comparative Analysis of Experiments in Different Geometries* (Forschungszentrum Jülich, 2012), vol. 14.
6. C. J. Jin *et al.*, Large-scale pedestrian flow experiments under high-density conditions. arXiv [Preprint] (2017). https://arxiv.org/pdf/1710.10263.pdf (Accessed 6 November 2021).
7. A. Johansson, Constant-net-time headway as a key mechanism behind pedestrian flow dynamics. *Phys. Rev. E Stat. Nonlin. Soft Matter Phys.* **80**, 026120 (2009).
8. D. Helbing, A. Johansson, H. Z. Al-Abideen, Dynamics of crowd disasters: An empirical study. *Phys. Rev. E Stat. Nonlin. Soft Matter Phys.* **75**, 046109 (2007).
9. A. Seyfried, B. Steffen, T. Lippert, Basics of modelling the pedestrian flow. *Physica A* **368**, 232–238 (2006).
10. A. Seyfried, B. Steffen, W. Klingsch, M. Boltes, The fundamental diagram of pedestrian movement revisited. *J. Stat. Mech.* **2005**, P10002 (2005).
11. U. Weidmann, Transporttechnik der fussgänger: Transporttechnische eigenschaften des fussgängerverkehrs, literaturauswertung. IVT Schriftenreihe 90 (1993). https://doi.org/10.3929/ethz-b-000242008. Accessed 6 November 2021.
12. M. Mori, H. Tsukaguchi, A new method for evaluation of level of service in pedestrian facilities. *Transp. Res. Part A Gen.* **21**, 223–234 (1987).
13. F. P. Navin, R. J. Wheeler, Pedestrian flow characteristics. Traffic Eng. Inst. Traffic Engr. 39, 30–36 (1969).
14. S. Older, Movement of pedestrians on footways in shopping streets. *Traffic Eng. Control* **10**, 160–163 (1968).
15. B. Hankin, R. A. Wright, Passenger flow in subways. *J. Oper. Res. Soc.* **9**, 81–88 (1958).
16. X. Ren, J. Zhang, W. Song, Flows of walking and running pedestrians in a corridor through exits of different widths. *Saf. Sci.* **133**, 105040 (2021).
17. J. J. Fruin, *Pedestrian Planning and Design* (Elevator World, 1987).
18. V. M. Predtechenskii, A. I. Milinskii, *Planning for Foot Traffic Flow in Buildings* (Amerind Publishing, 1978).
19. P. J. DiNenno, *SFPE Handbook of Fire Protection Engineering*, Society of Fire Protection Engineers (2008).
20. M. J. Hurley *et al.*, *SFPE Handbook of Fire Protection Engineering* (Springer, 2015).
21. D. Helbing, A mathematical model for the behavior of pedestrians. *Behav. Sci.* **36**, 298–310 (1991).
22. A. Garcimartín, J. M. Pastor, C. Martín-Gómez, D. Parisi, I. Zuriguel, Pedestrian collective motion in competitive room evacuation. *Sci. Rep.* **7**, 10792 (2017).
23. https://www.google.com/maps/d/viewer?mid=1zU4804rRF3S6z-8Hyz8Q3Q7bO-Q&ll=42.8179127889818%2C-1.6428772000000036&z=17/. Accessed 20 January 2021.
24. I. T. Jolliffe, *Principal Component Analysis* (Springer, 2002).
25. D. Helbing, B. A. Huberman, Coherent moving states in highway traffic. *Nature* **396**, 738–740 (1998).
26. Á. Garcimartín *et al.*, Redefining the role of obstacles in pedestrian evacuation. *New J. Phys.* **20**, 123025 (2018).
27. M. Moussaïd, D. Helbing, G. Theraulaz, How simple rules determine pedestrian behavior and crowd disasters. *Proc. Natl. Acad. Sci. U.S.A.* **108**, 6884–6888 (2011).
28. SanFerminEncierroTV, "Encierro de San Fermín - tapón en la plaza de toros de 1957" (video recording, 2012). https://www.youtube.com/watch?v=4q6Z2vxIPEw/. Accessed 20 January 2021.
29. SanFerminEncierroTV, "Encierro de San Fermín - 8 de julio de 1977" (video recording, 2012). https://www.youtube.com/watch?v=Jkou4uexgdI/. Accessed 20 January 2021.
30. RTV TOROS, "Septimo Encierro San Fermín 13-7-2013 Explicación del encierro gracias a Manolo Molés" (video recording, 2013). https://www.youtube.com/watch?v=ilShtXwKVFI/. Accessed 20 January 2021.
31. M. Zrenner, S. Gradl, U. Jensen, M. Ullrich, B. M. Eskofier, Comparison of different algorithms for calculating velocity and stride length in running using inertial measurement units. *Sensors (Basel)* **18**, 4194 (2018).
32. A. Nummela, T. Keränen, L. O. Mikkelsson, Factors related to top running speed and economy. *Int. J. Sports Med.* **28**, 655–661 (2007).
33. S. Yan, J. Jin, "Study on stride length, rate, and speed of 100m sprint running with five kinds of speed" in *Proceedings of the 22nd International Symposium on Biomechanics in Sports* (ISBS-Conference Proceedings Archive, 2004) pp. 318–321.
34. A. Nicolas, M. Kuperman, S. Ibañez, S. Bouzat, C. Appert-Rolland, Mechanical response of dense pedestrian crowds to the crossing of intruders. *Sci. Rep.* **9**, 105 (2019).
35. G. F. Newell, Nonlinear effects in the dynamics of car following. *Oper. Res.* **9**, 209–229 (1961).
36. G. Baglietto, D. R. Parisi, Continuous-space automaton model for pedestrian dynamics. *Phys. Rev. E Stat. Nonlin. Soft Matter Phys.* **83**, 056117 (2011).
37. G. Bradski, Dr. Dobb's journal: Software tools for the professional programmer **25**, 120–123 (2000). https://docs.opencv.org/3.4/da/d54/group__imgproc__transform.html#ga55c716492470bfe86b0ee9bf3a1f0f7e. Accessed 24 July 2021.
38. D. F. Specht, A general regression neural network. *IEEE Trans. Neural Netw.* **2**, 568–576 (1991).
39. D. R. Parisi, D. Sornette, D. Helbing, Financial price dynamics and pedestrian counterflows: A comparison of statistical stylized facts. *Phys. Rev. E Stat. Nonlin. Soft Matter Phys.* **87**, 012804 (2013).
40. G. A. Patterson, D. Sornette, D. R. Parisi, Properties of balanced flows with bottlenecks: Common stylized facts in finance and vibration-driven vehicles. *Phys. Rev. E* **101**, 042302 (2020).
41. B. Steffen, A. Seyfried, Methods for measuring pedestrian density, flow, speed and direction with minimal scatter. *Phys. A Stat. Mech.* **389**, 1902–1910 (2010).